nature portfolio

https://doi.org/10.1038/s41596-023-00806-x

Supplementary information

iBEAT V2.0: a multisite-applicable, deep learning-based pipeline for infant cerebral cortical surface reconstruction

In the format provided by the authors and unedited

Supplementary File for

iBEAT V2.0: A Multi-site Applicable, Deep Learning-based Pipeline for Infant Cerebral Cortical Surface Reconstruction

Li Wang[#,*], Zhengwang Wu[#,*], Liangjun Chen, Yue Sun, Weili Lin, Gang Li*, for UNC/UMN Baby Connectome Project Consortium

Department of Radiology and BRIC, University of North Carolina at Chapel Hill, NC 27599, USA

[#] Co-first authors, [*] Co-corresponding authors

1. Procedure Method Details

1.1 Image Preprocessing

Since the brain MR images are 3D images, the data can be organized using different slicing strategies, which will cause inconsistency when doing the computation. Therefore, whenever comes a new image, we need first to make sure the brain data is sliced using the same strategy. Because the original slicing strategy has been recorded in the image meta information, we only need to reorient the image. As illustrated in the first step of the procedure section in the main paper, in iBEAT V2.0, the first dimension index of the volume corresponds to the sagittal slices, which goes from left to right as the index increases; The second dimension index corresponds to the coronal slices, which goes from posterior to anterior as the index increases; And the third dimension index corresponds to the transverse slices, which goes from inferior to superior as the index increases. Fig. S1 shows a typical brain MR image before and after reorientation. Before reorientation, the first dimension index corresponds to the coronal slices. And after reorientation, the first dimension index corresponds to the sagittal slices. After reorientation, T2w image is rigidly aligned into its T1w image space if both T1w and T2w images are available, by using FLIRT [16,17] from FSL.

Due to the inherent non-uniformity of the magnetic field of MR scanners, the intensity of the brain volume is overlayed with a smooth but regionally heterogeneous bias field, which shifts intensity values and leads to spatially-dependent imaging appearances, i.e., the same brain would have different imaging appearances due to different positions inside the same MR scanner. This would introduce unwanted extra imaging appearance variations for subsequent processing. Therefore, it is beneficial to remove the bias field in the preprocessing stage. Fortunately, we can remove it using sophisticated algorithms, such as the N3[1] and N4[2] algorithms.

Theoretically, there are two modifications between N3 and N4. 1) The interpolation method for the bias field generation used in N4 is a hierarchical strategy, which gradually increases the B-spline control points at each iteration, whereas N3 uses a fixed number of control points; 2) N4 estimates the residual of the bias field after each iteration, while N3 estimate a new bias field at each iteration.

The first one is for handling the inappropriate input distance parameter of the N3 method. However, when this parameter is in an appropriate range, their performance is similar. This conclusion has been discussed in both N3 [1] and N4 [2]. In the N3 paper [1], the authors have validated the sensitivity of this parameter and showed the bias field correction is not sensitive when this parameter is in a reasonable range. In our pipeline, we used the suggested distance (control points number) parameter of the N3 method, which consistently leads to reasonable bias field estimations.

The second one can improve the convergence of the N3 method. Basically, N4 does several rounds of bias field correction. The output of the previous round is fed into the current round. Thus, the current round only needs to estimate the residual bias field, which improves the performance. We are also aware of this strategy. Therefore, we actually used N3 in a similar residual estimation manner as N4 by running N3 for three rounds in our pipeline.

Fig. S1. An image slice along the first dimension index before and after reorientation.

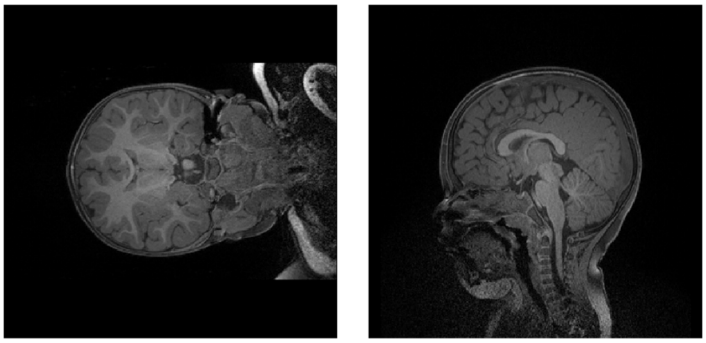

Left: the image slice before reorientation, which corresponds to the coronal slice; Right: the image slice after reorientation, which corresponds to the sagittal slice.

Based on our experiences, setting the default distance parameter and running N3 three times achieves similar performance with N4. In addition, as we trained our models based on training images corrected by N3, to be consistent with the training, we used the N3 method for removing the bias field for testing subjects. In the future, we will also train an N4-based model, which will enable users more flexibility.

1.2 Skull Stripping and Cerebellum Removal

As our focus is on morphometric measurements of the cerebrum, the non-cerebral structures, e.g., the brain skull and cerebellum, are removed before subsequent processing. Specifically, we first perform skull stripping to remove non-brain structures, including head-neck tissues, brain skull, scalp, and dura. Then, we further remove the cerebellum from the skull-stripped brain image.

Many skull stripping and cerebellum removal methods have been proposed [3–10]. However, these methods are mainly developed for adult brain images, which have relatively consistent imaging appearance and good contrast. To handle the dynamic appearance and low contrast in infant brain images, we formulate skull stripping and cerebellum removal as two segmentation problems.

For skull stripping, given a local 3D patch from the intensity inhomogeneity-corrected image, we determine whether it belongs to the brain region (foreground) or the non-brain region (background). As the intensities of non-brain regions are relatively consistent across ages, we train a single network model [11] based on all the training images from different ages. Specifically, we feed the extracted T1w and/or T2w local patches together with their labels, i.e., the brain or non-brain, to the network. Then, the network learns a highly nonlinear mapping. Given a new patch, the learned mapping can be used to predict whether the patch center is from brain or non-brain regions. We used a deep learning method, i.e., the densely connected U-net [11], as the learning network, whose structure is illustrated in Fig. S2 (also used for the tissue segmentation in the next section). Herein, the patch size is 64x64x64, which carries enough appearance information for the network training across the infancy based on our experience. All training patches are augmented with random rotation and flip to enlarge the generalization ability. Similarly, for cerebellum removal, we also train a similar network as illustrated in Fig. S2 [11]. The difference is that, herein, the local patch is extracted from the skull-stripped images and the label indicates whether its center is from the cerebrum or the cerebellum. Notably, in the network training, we assign a large weight loss for the boundaries between the foreground and background, as accurate identification is more important for the boundaries than for other regions.

1.3 Tissue Segmentation

Tissue segmentation, which is one of the most challenging tasks in infant MRI processing, aims to accurately segment the cerebrum into three tissue types, i.e., gray matter (GM), white matter (WM), and cerebrospinal fluid (CSF). Tissue segmentation is challenging for three major reasons: a) the appearance pattern of the same tissue type varies across different age groups due to the undergoing myelination process; b) the image contrast among different tissues during infancy is extremely low, especially in the 6-month-old brain; and c) the cerebral cortex is a highly convoluted structure with large inter-subject variability and is only few voxels in thickness.

Fig. S2. Diagram of the densely connected network structure.

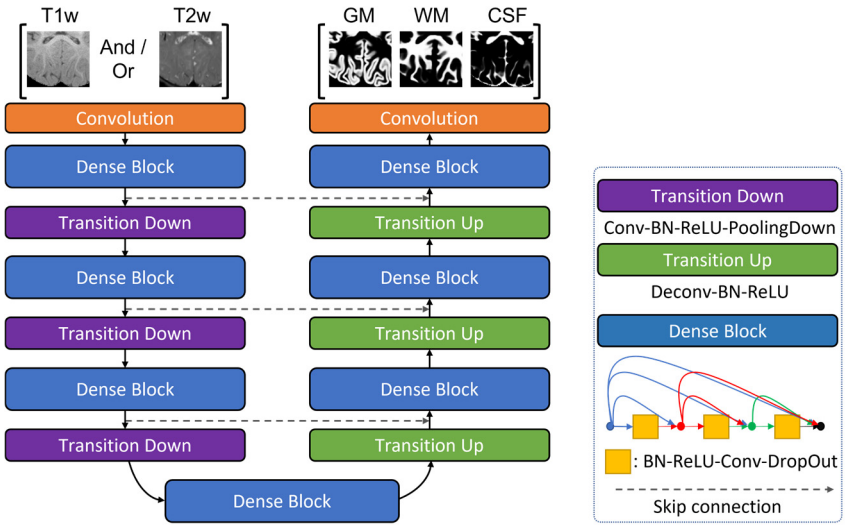

The detailed structure of the densely connected network used in the segmentation tasks in the iBEAT V2.0 pipeline (GM: gray matter; WM: white matter; CSF: cerebrospinal fluid).

To address these challenges, instead of training a single neural network model for all age groups like skull stripping, we train a specialized deep learning-based tissue segmentation model for each representative age group. Specifically, we train the segmentation models at the neonatal stage (<=1 month), 3 months, 6 months, 9 months, 12 months, 18 months, and >=24 months of age. The motivation for this training strategy is that brain images within each of these age groups generally present highly representative and relatively consistent appearances. This age group partition strategy has been extensively verified to improve segmentation performance in many previous studies [12–15].

Herein, we use a novel densely connected U-net as the backbone segmentation network. Notably, this densely connected U-net is also used for skull stripping and cerebellum removal in our pipeline. The network architecture is presented in Fig. S2, which includes a down-sampling path and an up-sampling path, going through seven dense blocks. Each dense block consists of 3 BN-ReLU-Conv-Dropout operations (BN stands for the batch normalization, ReLU stands for the rectified linear activation unit, and Conv stands for the convolution), in which Conv includes 16 kernels (3x3x3 with stride 1 and 0 padding) and the dropout rate is 0.1. In the down-sampling path, between any two continuous dense blocks, a transition down block (i.e., Conv-BN-ReLU followed by a max-pooling layer) is included to downsample the feature maps and increase the receptive field; while in the upsampling path, a transition up block, consisting of a transposed convolution, is included between any two continuous dense blocks to upsample the feature maps from the preceding dense block. The up-sampled feature maps are then concatenated with the same level feature maps in the down-sampling path and fed into the subsequent dense block to compensate for the information lost due to the reduced resolution. In the last layer, a softmax layer is adopted to estimate the tissue probabilities for each voxel.

In the *training stage*, for each image from each age group, we first normalize the image by matching its intensity histogram to that of the corresponding age-specific template. Then, we sample patches (with a size of 32x32x32) around different tissue boundaries, and these sampled patches are further rotated and flipped for data augmentation. After that, the originally sampled patches, together with the augmented patches, are fed into the network to train the model in a patch-wise manner. In the *testing stage*, we first match the intensity histogram of the testing image with the age-matched template. Then, each patch from the histogram-matched image is fed into the trained age-matched model for the prediction of tissue labels.

1.4 Hemisphere Separation and Noncortical Region Filling

To better characterize medial cortical structures and leverage the spherical topology, the cerebrum is split into the left and right hemispheres, and subcortical regions and lateral ventricles are filled with white matter to facilitate surface reconstruction. We split the brain into the left and right hemispheres by registration of an age-matched template onto the individual brain. The labels of hemispheres, subcortical regions and ventricles in the template are propagated to the individual brain based on the obtained deformation field. We have constructed the infant brain atlases at different age groups, including 1, 3, 6, 9, 12, 18, and 24 months of age. For each age group, the atlas includes the labels of the left and right hemispheres. Fig. S3 shows a typical example of the atlas image and its corresponding hemispherical labels for 24-month-old age group.

To propagate hemispheric labels from the age-matched atlas onto each individual brain, we first linearly align the atlas intensity image onto the individual intensity image and accordingly bring the hemisphere labels on the atlas into the individual brain. This is achieved by first labeling WM voxels and then expanding WM labels into adjacent GM and CSF. Herein, a linear registration is adequate because this step only requires the position and orientation of the brain to be aligned. The linear registration tool we used is FLIRT [16,17] from FSL.

Fig. S3. Left and right hemisphere separation atlas.

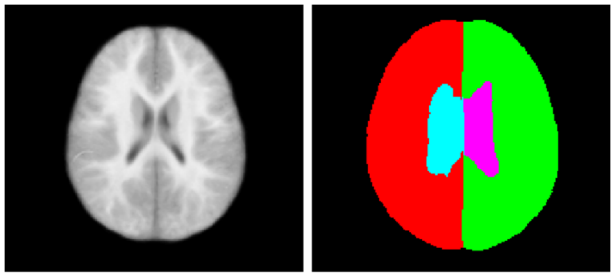

(a) (b)

The intensity atlas (a) and the corresponding left and right hemisphere labels. The subcortical regions and the lateral ventricles are also labeled in the atlas (in magenta and cyan colors).

1.5 Topological Correction

While embedded in 3D space, the cortical surfaces of each hemisphere should be topologically equivalent to a sphere, i.e., a 2D closed surface, in essence. However, due to the low tissue contrast and dynamic imaging appearance of the infant brain images, some voxels are often incorrectly labeled in the segmentation map. This can cause two types of topological errors/defects, i.e., 1) holes; and 2) bridges/handles, as shown in Fig. 3 (e). A hole refers to a perforation on the gyrus, and a handle refers to an erroneous bridge connecting two neighboring gyri. Such errors will result in an incorrect topology of the reconstructed cortical surface, causing problems when mapping the cortical surface onto a sphere or flattening it into a plane, leading to inaccurate geodesic, morphological and connectivity

measurements of the cortical surfaces. Therefore, such topological errors need to be corrected before reconstructing the cortical surfaces [18–21]. Of note, researchers typically first correct topological errors on the inner surface and then deform the corrected inner surface to reconstruct the middle and outer/pial surfaces, which often cannot be directly reconstructed due to severe partial volume effects in deep tight sulci in infant images. This strategy will ensure correct topology and vertex-to-vertex correspondences for inner, middle, and outer/pial cortical surfaces.

To avoid topological errors, we first need to locate where the errors are and then correct them. However, holes and handles on the cortical surface are difficult to distinguish by solely relying on geometric and intensity information. To address this issue, we can employ a learning-based method to adaptively correct the detected topological errors [22]. Specifically, for each hemisphere, we first deform an initial surface with a sphere topology (i.e., an ellipsoid) to closely wrap the segmented white matter volume, while preserving its initial topology, using a shrinking-wrapping topology-preserving level set method [23]. Then, we identify the defect regions as locations where the converged surface mismatches the original white matter surface. To correct the defect regions, we learn a correction model from training samples that have been manually edited by experts, and then apply the learned model to new subjects. Specifically, a deep convolutional neural network can be leveraged to learn the strategy to correct labels in local image patches in defect regions. To correct large and complex handles or holes, we further incorporate the steps of localization and correction of defects into an iterative framework [22].

1.6 Cortical Surface Reconstruction

After correction of topological errors, we reconstruct cortical surfaces, represented by triangular meshes, by first reconstructing the inner surface and then reconstructing the middle and outer/pial surfaces. Specifically, we use the marching cubes tessellation method [24] to represent the boundary of the topologically correct white matter volume as a triangular surface mesh and further smooth and deform the surface mesh to remove bumpy and spike cusps to obtain a topologically correct and geometrically accurate inner cortical surface. Then, we deform the inner surface toward the gray matter/CSF boundary to obtain the outer surface. This deformation process needs to be performed with caution because of the following challenges. First, due to the underlying myelination process, the infant brain image has extremely low tissue contrast, which means that the boundaries between neighboring tissues are usually ambiguous. Second, due to the severe partial volume effects, especially in deep sulcal regions, the distances between opposing sulcal banks are often smaller than the MRI resolution, and the CSF can hardly be seen, thus making outer surface reconstruction in the deep sulci very challenging. Third, the infant cerebral cortex expands rapidly, even in a relatively small-time interval. Therefore, for the same infant, the reconstructed cortical surfaces at different time points are potentially inconsistent, resulting in temporally inconsistent and inaccurate measurements of longitudinal brain development.

To address the low tissue contrast issue, instead of depending on the unreliable and noisy intensity gradient vector field to deform the cortical surface, we base the external force for driving surface deformation on the Laplacian equation and the topology-corrected tissue map. This leads to a more reliable driving force for surface deformation, as the topology-corrected tissue map is obtained not only based on intensity gradient information, but also on more informative contextual features and anatomical and topological prior knowledge. In addition to the external force, we employ an internal force to keep the surface tight and smooth when deforming it [25,26].

To generate an accurate outer cortical surface in deep sulci, we first recover the CSF in deep sulci using the anatomically consistent enhancement method [27–29] to generate a no-more-than-one-voxel thick separation between opposite sulcal banks. Then, before entering the recovered CSF regions, we deform the cortical surface using both internal and external forces. After entering the recovered CSF regions, instead of relying on external force based on tissue maps, we employ the local normal direction of the surface to define the external force to make the opposing sulcal banks closely approach each other. To ensure spherical topology and avoid triangle self-intersections on the outer surface, we

explicitly check the potential triangle-triangle intersections [30] in each step of surface deformation and reduce the deformation step size accordingly. Thus, the inner and outer surfaces have the same spherical topology and vertex-to-vertex correspondences. The middle surface is then generated as the geometric mean of the inner and outer surfaces. In longitudinal studies, to further address the potential temporal inconsistency at different time points, we can jointly deform the longitudinal surfaces of the same subject, with an additional explicit force to encourage temporal consistency [25]. Fig. 4 shows the reconstructed inner and outer cortical surfaces (color-coded by cortical thickness) overlayed on corresponding T1w MR images at different ages. The reconstructed cortical surfaces are well aligned with the tissue boundaries.

1.7 Cortical Measurement

Once cortical surfaces are reconstructed, we compute multiple biologically distinct and meaningful cortical properties for each vertex, e.g., cortical thickness, surface area, myelin content, sulcal depth, gyrification index, and curvatures, to comprehensively characterize the complex development of the cerebral cortex during infancy.

Specifically, for each vertex, the cortical thickness is computed as the minimum distance between the inner and outer surfaces. The surface area is computed as one-third of the summed area of all triangles associated with a vertex on the middle cortical surface for a more balanced representation of sulci and gyri. The myelin content is computed as the T1w/T2w ratio (before intensity inhomogeneity correction) on the middle cortical surface, reflecting the myeloarchitecture of the cortex [31]. The sulcal depth is computed as the distance from the outer surface to the nearest point on the cerebral hull surface, which tightly wraps the brain, to characterize both coarse and fine cortical shape information. The gyrification index is the areal ratio of the outer surface and the cerebral hull surface, and the local gyrification index is the areal ratio between a local region on the outer surface and the corresponding region on the cerebral hull surface. The mean curvature reflects the fine-scale local geometric properties of cortical folding and is computed as the average of the minimum and maximum principal curvatures, which can be further used to derive the Gaussian curvature, shape index, and curvedness for characterizing local cortical folding.

Notably, the reconstructed cortical surfaces also provide a framework for mapping and integration of brain structural, functional, and connectivity properties from multimodal images for a comprehensive investigation of early brain development. For example, in functional MRI, functional signals can be mapped onto the middle cortical surface to evaluate functional connectivity, gradients, and regional homogeneity; in diffusion MRI, diffusivity information can be mapped onto the middle cortical surface to evaluate the cortical microstructure, and white matter fibers can be mapped onto the inner surface to evaluate cortical structural connectivity.

2. Preliminary Results on Subcortical Region Segmentation

We are actively developing the subcortical structure segmentation tools by training a model that is robust to different imaging protocols and scanners, as we did for the cortex region. We mainly focus on 6 subcortical regions in each hemisphere, i.e., the hippocampus, amygdala, putamen, pallidum, caudate, and thalamus. In the current stage, we have achieved some preliminary results, as reported in Fig. S4 and Table S1. However, we still need more training samples and validations to make the subcortical segmentation more reliable. Once it works robustly on diverse images, we will incorporate the subcortical segmentation module into our pipeline too.

Table S1. Subcortical segmentation evaluation on the BCP dataset.						
Dice ratio (Mean±Std.)	Thalamus	Caudate	Putamen	Pallidum	Hippocampus	Amygdala
Neonates	0.95±0.01	0.91±0.02	0.92±0.02	0.85±0.03	0.88±0.03	0.86±0.04
6 Months	0.96±0.02	0.94±0.02	0.93±0.02	0.92±0.02	0.90±0.02	0.86±0.03
12 Months	0.96±0.01	0.95±0.01	0.95±0.01	0.95±0.01	0.91±0.02	0.88±0.02
24 Months	0.97±0.01	0.95±0.01	0.94±0.02	0.94±0.01	0.91±0.02	0.89±0.02

Fig. S4. Typical subcortical segmentation results on the BCP dataset.

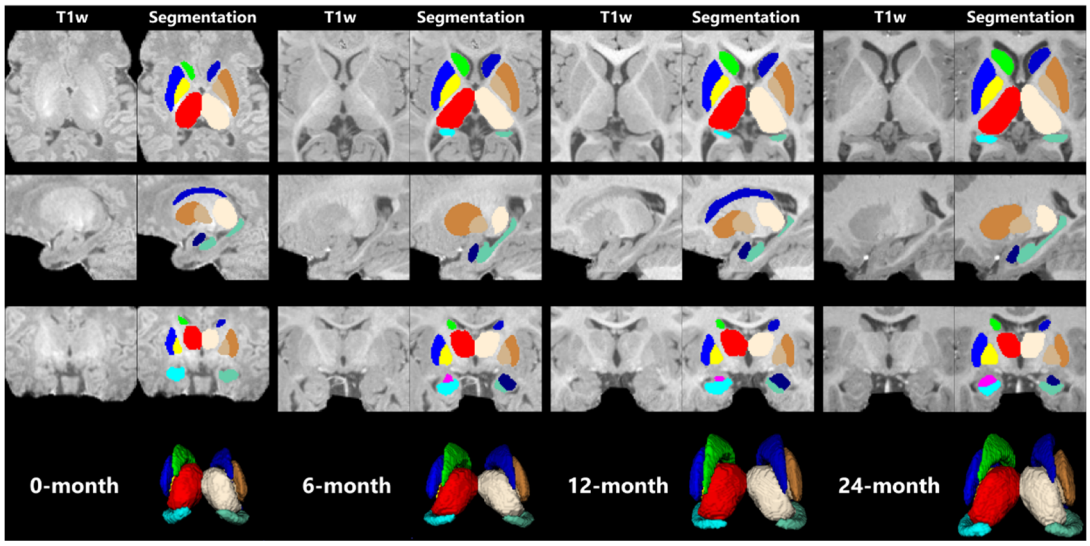

Demonstration of the subcortical segmentations for 4 BCP subjects at 0, 6, 12, and 24 months of age. The first three rows show the transversal view, sagittal view, and coronal view, respectively. The last row shows the subcortical surface rendering.

3. Additional Views of Pipeline Evaluation

For a more comprehensive illustration, we have provided different views of the brains and their processing results. Fig. S5 includes the sagittal and coronal views of the proposed pipeline framework in Fig. 3. While Figs. S6 and S7 show the sagittal and coronal views of Extended Data Fig. 1, respectively.

Fig. S5. The framework of the iBEAT V2.0 computational pipeline.

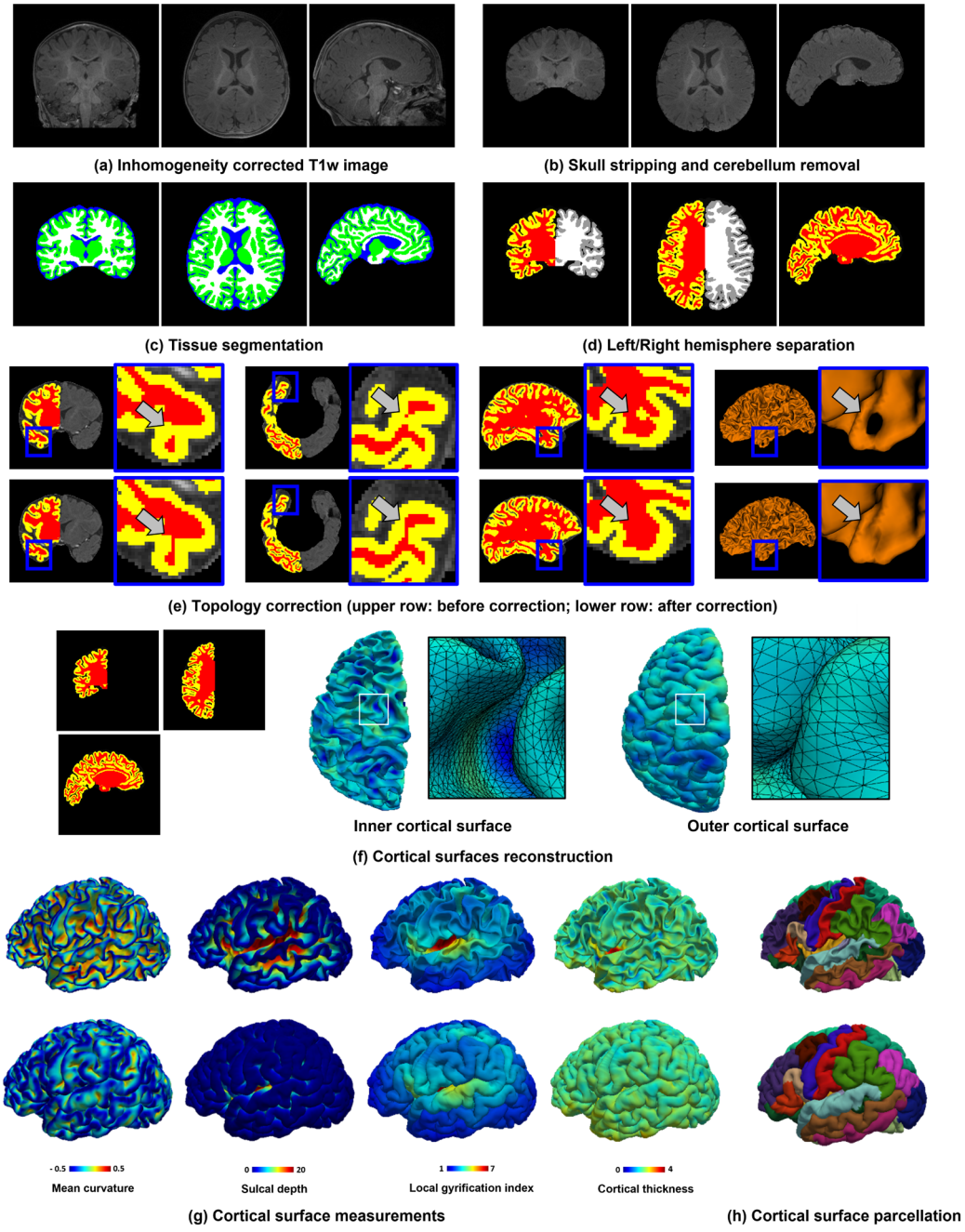

The iBEAT V2.0 pipeline includes *an image segmentation component*: (a) Input inhomogeneity-corrected T1w image (also applicable to T2w images, or both), (b) T1w image after skull stripping and cerebellum removal, and (c) Tissue segmentation map, with green indicating gray matter, white indicating white matter, and blue indicating cerebrospinal fluid; and *a cortical surface reconstruction component*: (d) Left/right hemisphere separation and filling of the noncortical regions with white matter, (e) Topology correction of white matter volume, (f) Reconstructed inner and outer cortical surfaces represented by triangular meshes, (g) Color-coded derived representative cortical properties, e.g., mean curvature, sulcal depth, local gyrification index, and cortical thickness, and (h) Parcellated cortical surfaces based on Desikan scheme. All images in figure are shown in 3 different views for better inspection.

Fig. S6. Comparison of processing results between Infant FreeSurfer and iBEAT V2.0 on different datasets in sagittal view.

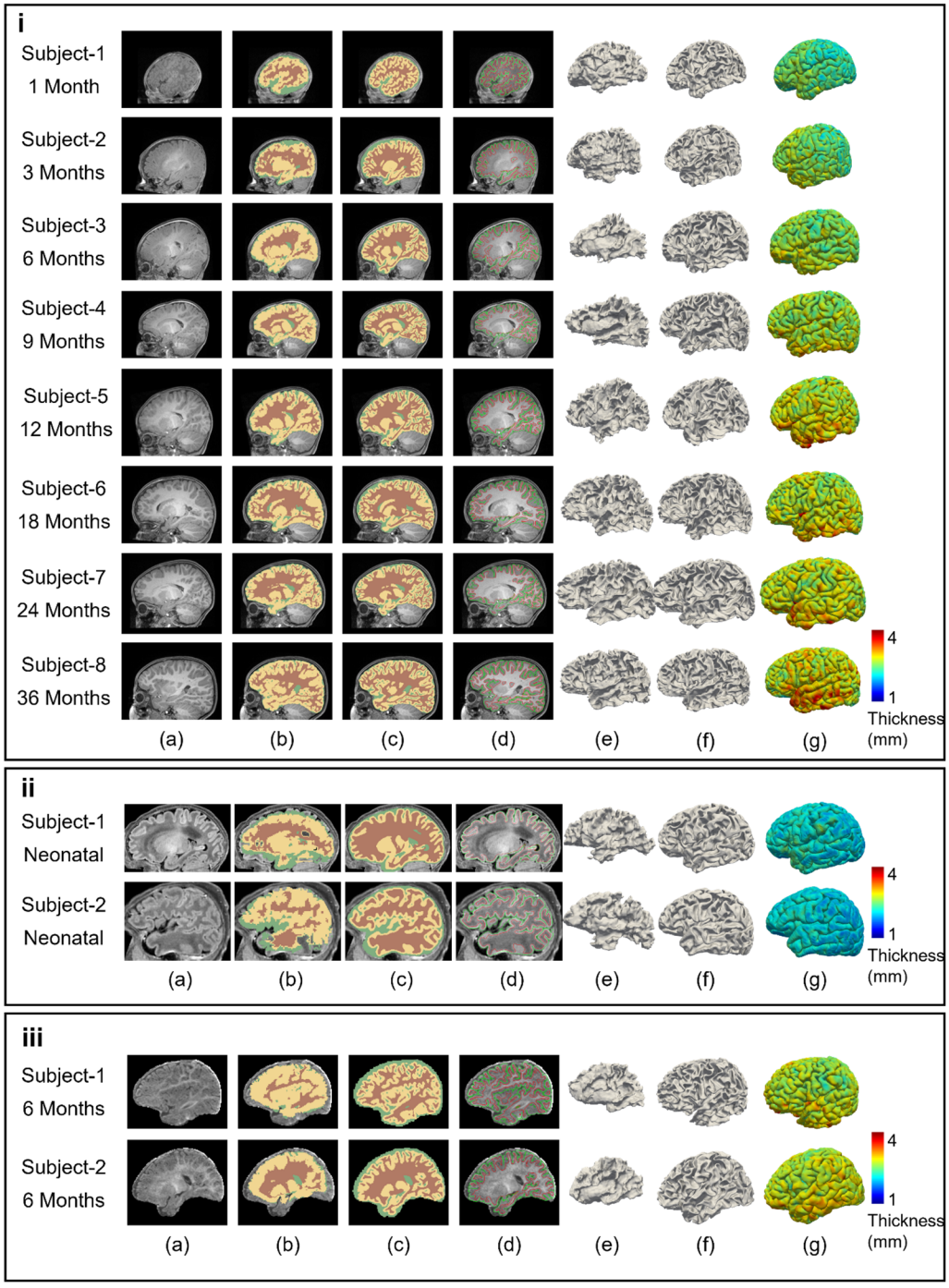

i. Comparison on BCP dataset. ii. Comparison on dHCP dataset. iii. Comparison on MSMS dataset. (a) T1w image. (b) Tissue segmentation by Infant FreeSurfer. (c) Tissue segmentation by iBEAT V2.0. (d) iBEAT V2.0 reconstructed cortical surfaces overlayed on intensity images, with red contours indicating the inner surface and green contours indicating the outer surface. (e) Reconstructed inner cortical surface using Infant FreeSurfer. (f) Reconstructed inner cortical surfaces using iBEAT V2.0. (g) Reconstructed outer cortical surfaces (color-coded by cortical thickness) using iBEAT V2.0.

Fig. S7. Comparison of processing results between Infant FreeSurfer and iBEAT V2.0 on different datasets in coronal view.

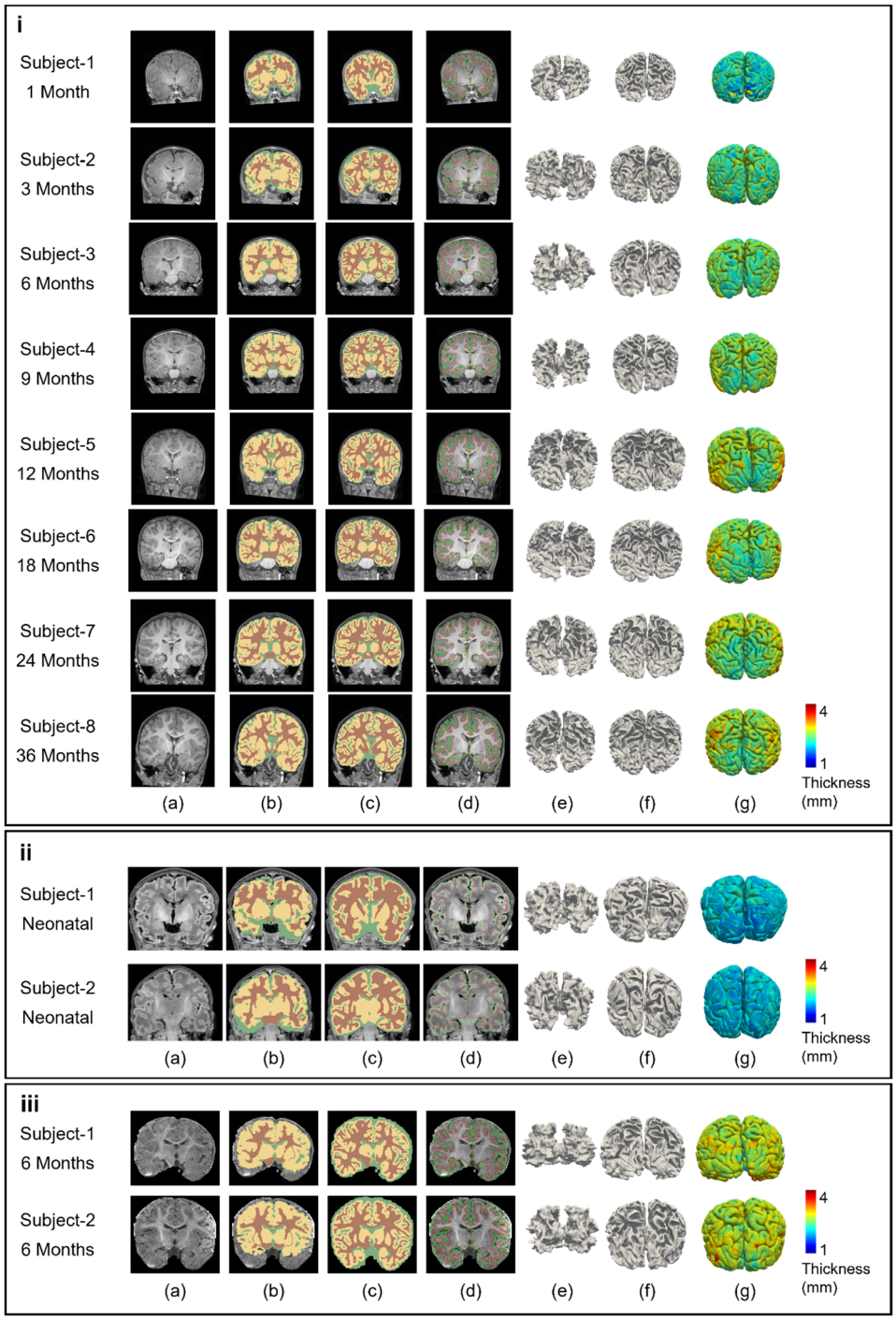

i. Comparison on BCP dataset. ii. Comparison on dHCP dataset. iii. Comparison on MSMS dataset. (a) T1w image. (b) Tissue segmentation by Infant FreeSurfer. (c) Tissue segmentation by iBEAT V2.0. (d) iBEAT V2.0 reconstructed cortical surfaces overlayed on intensity images, with red contours indicating inner surface and green contours indicating outer surface. (e) Reconstructed inner cortical surface using Infant FreeSurfer. (f) Reconstructed inner cortical surfaces using iBEAT V2.0. (g) Reconstructed outer cortical surfaces (color-coded by cortical thickness) using iBEAT V2.0.

4. Screenshot of the pipeline usage.

There are two ways to use the iBEAT V2.0 pipeline. One way is to upload the images to the cloud version (www.ibeat.cloud). The other way is to download and install the Docker version of the iBEAT V2.0 (https://github.com/iBEAT-V2/iBEAT-V2.0-Docker), then image processing can be conducted on a local computer.

Fig. S8. Screenshots of using the pipeline in cloud version and Docker version.

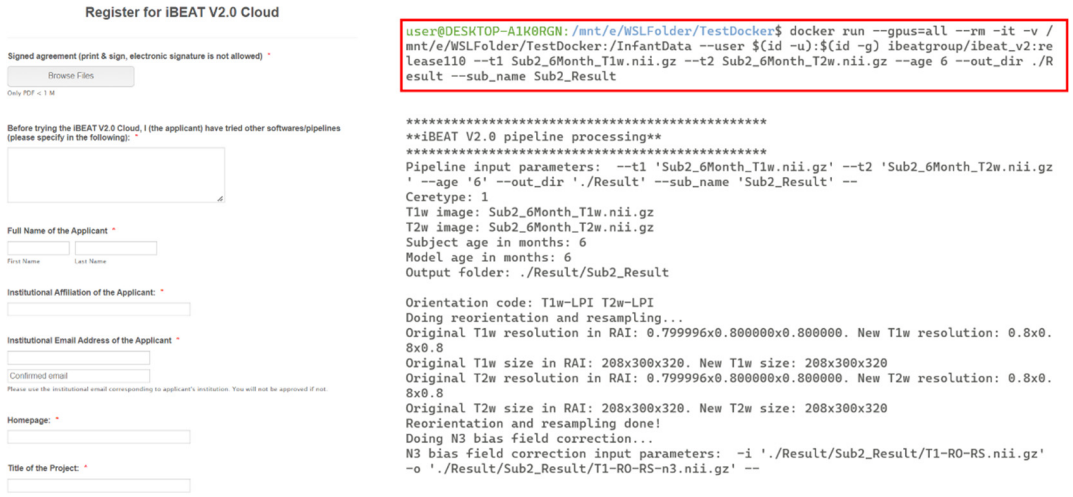

(a) (b)

(a) Using the pipeline on the iBEAT Cloud (www.ibeat.cloud). The user needs to fill out this form to register and upload the data. Once the data is uploaded, the pipeline will process the data and return the processed results to the user's registered email. (b) Using the Docker version of the pipeline. The Docker version of the pipeline can be accessed through the instructions on https://github.com/iBEAT-V2/iBEAT-V2.0-Docker. Once downloaded and installed, the user can use the command in the red box to process the images on a local computer.

5. Reliability of cortical thickness during infancy

It is a common problem[31–34] that measuring the cortical thickness can be influenced by the heterogeneous myelination either across different ages of the same subject or across different subjects, which leads to the variable contrast at gray matter and white matter boundaries in MRI, especially in the infant brains with dynamic development, thin cortex and limited imaging resolution. To address this issue, we *learn age-dependent models for typical infant age groups to consistently achieve excellent tissue segmentation performance.* Specifically, we first group the brain images based on their ages so that the images inside the same age group would have substantially smaller image contrast variability. Then, we leverage the powerful deep learning strategy to learn a highly nonlinear mapping from the image appearance pattern to the specific tissue types. Benefiting from the powerful mapping ability by deep learning, we achieved consistently high tissue segmentation accuracy for different infant age groups, which has been validated by 16,000+ infant brain images from 100+ institutions. Finally, based on high-quality tissue maps, we consistently reconstruct the inner and outer cortical surfaces across ages using the same deformable surface method and accordingly measure the cortical thickness. Therefore, we believe the cortical thickness measurements computed by our pipeline are reliable and comparable at different ages. However, the accuracy of cortical thickness could be further improved with more advanced methods and higher resolution MR images.

References

1. Sled, J. G., Zijdenbos, A. P. & Evans, A. C. A nonparametric method for automatic correction of intensity nonuniformity in mri data. *IEEE Trans. Med. Imaging* **17**, 87–97 (1998).

2. Tustison, N. J. *et al.* N4ITK: Improved N3 bias correction. *IEEE Trans. Med. Imaging* **29**, 1310–1320 (2010).

3. Shi, F. *et al.* LABEL: Pediatric brain extraction using learning-based meta-algorithm. *Neuroimage* **62**, 1975–1986 (2012).

4. Shattuck, D. W., Prasad, G., Mirza, M., Narr, K. L. & Toga, A. W. Online resource for validation of brain segmentation methods. *Neuroimage* **45**, 431–439 (2009).

5. Smith, S. M. Fast robust automated brain extraction. *Hum. Brain Mapp.* **17**, 143–155 (2002).

6. Sadananthan, S. A., Zheng, W., Chee, M. W. L. & Zagorodnov, V. Skull stripping using graph cuts. *Neuroimage* **49**, 225–239 (2010).

7. Soussia, M. *et al.* A computational framework for dissociating development-related from individually variable flexibility in regional modularity assignment in early infancy. in *International Conference on Medical Image Computing and Computer-Assisted Intervention* vol. 12267 LNCS In Press (Springer Science and Business Media Deutschland GmbH, 2020).

8. Zhang, Q. *et al.* FRNET: Flattened Residual Network for Infant MRI Skull Stripping. in *IEEE International Symposium on Biomedical Imaging* vols 2019-April 999–1002 (IEEE, 2019).

9. Han, S., Carass, A., He, Y. & Prince, J. L. Automatic cerebellum anatomical parcellation using U-Net with locally constrained optimization. *Neuroimage* **218**, 116819 (2020).

10. Sun, Y. *et al.* Semi-supervised Transfer Learning for Infant Cerebellum Tissue Segmentation. in *International Workshop on Machine Learning in Medical Imaging* vol. 12436 LNCS 663–673 (Springer, 2020).

11. Wang, L. *et al.* Volume-Based Analysis of 6-Month-Old Infant Brain MRI for Autism Biomarker Identification and Early Diagnosis. in *International Conference on Medical Image Computing and Computer-Assisted Intervention* vol. 11072 LNCS 411–419 (Springer, 2018).

12. Nie, D. *et al.* 3-D Fully Convolutional Networks for Multimodal Isointense Infant Brain Image Segmentation. *IEEE Trans. Cybern.* **49**, 1123–1136 (2019).

13. Makropoulos, A., Counsell, S. J. & Rueckert, D. A review on automatic fetal and neonatal brain MRI segmentation. *Neuroimage* **170**, 231–248 (2018).

14. Wang, L. *et al.* LINKS: Learning-based multi-source IntegratioN frameworK for Segmentation of infant brain images. *Neuroimage* **108**, 160–172 (2015).

15. Li, G. *et al.* Computational neuroanatomy of baby brains: A review. *Neuroimage* **185**, 906–925 (2019).

16. Jenkinson, M. & Smith, S. A global optimisation method for robust affine registration of brain images. *Med. Image Anal.* **5**, 143–156 (2001).

17. Jenkinson, M., Bannister, P., Brady, M. & Smith, S. Improved Optimization for the Robust and Accurate Linear Registration and Motion Correction of Brain Images. *Neuroimage* **17**, 825–841 (2002).

18. Shattuck, D. W. & Leahy, R. M. Brainsuite: An automated cortical surface identification tool. *Med. Image Anal.* **6**, 129–142 (2002).

19. Glasser, M. F. *et al.* The minimal preprocessing pipelines for the Human Connectome Project.

Neuroimage **80**, 105–124 (2013).

20. Makropoulos, A. *et al.* The developing human connectome project: A minimal processing pipeline for neonatal cortical surface reconstruction. *Neuroimage* **173**, 88–112 (2018).

21. Fischl, B., Sereno, M. I. & Dale, A. M. Cortical surface-based analysis: II. Inflation, flattening, and a surface-based coordinate system. *Neuroimage* **9**, 195–207 (1999).

22. Sun, L. *et al.* Topological correction of infant white matter surfaces using anatomically constrained convolutional neural network. *Neuroimage* **198**, 114–124 (2019).

23. Han, X., Xu, C. & Prince, J. L. A topology preserving level set method for geometric deformable models. *IEEE Trans. Pattern Anal. Mach. Intell.* **25**, 755–768 (2003).

24. Lorensen, W. E. & Cline, H. E. MARCHING CUBES: A HIGH RESOLUTION 3D SURFACE CONSTRUCTION ALGORITHM. *Comput. Graph.* **21**, 163–169 (1987).

25. Li, G., Nie, J., Wu, G., Wang, Y. & Shen, D. Consistent reconstruction of cortical surfaces from longitudinal brain MR images. *Neuroimage* **59**, 3805–3820 (2012).

26. Li, G. *et al.* Measuring the dynamic longitudinal cortex development in infants by reconstruction of temporally consistent cortical surfaces. *Neuroimage* **90**, 266–279 (2014).

27. Li, G., Guo, L., Nie, J. & Liu, T. An automated pipeline for cortical sulcal fundi extraction. *Med. Image Anal.* **14**, 343–359 (2010).

28. Perrot, M., Rivière, D. & Mangin, J. F. Cortical sulci recognition and spatial normalization. *Med. Image Anal.* **15**, 529–550 (2011).

29. Han, X. *et al.* CRUISE: Cortical reconstruction using implicit surface evolution. *Neuroimage* **23**, 997–1012 (2004).

30. Moller, T. & AB, P. clarus. A Fast Triangle-Triangle Intersection Test. *ournal Graph. GPU, Game Tools* **2**, 25–30 (1997).

31. Glasser, M. F. & van Essen, D. C. Mapping human cortical areas in vivo based on myelin content as revealed by T1- and T2-weighted MRI. *J. Neurosci.* **31**, 11597–11616 (2011).

32. Sowell, E. R. *et al.* Longitudinal mapping of cortical thickness and brain growth in normal children. *J. Neurosci.* **24**, 8223–8231 (2004).

33. Li, G., Lin, W., Gilmore, J. H. & Shen, D. Spatial patterns, longitudinal development, and hemispheric asymmetries of cortical thickness in infants from birth to 2 years of age. *J. Neurosci.* **35**, 9150–9162 (2015).

34. Huang, Y. *et al.* Mapping developmental regionalization and patterns of cortical surface area from 29 post-menstrual weeks to 2 years of age. *Proc. Natl. Acad. Sci.* **119**, e2121748119 (2022).